Received June 18, 2020, accepted July 14, 2020, date of current version August 4, 2020.

Digital Object Identifier 10.1109/ACCESS.2020.3011224

A New Hybrid Brain MR Image Segmentation Algorithm With Super-Resolution, Spatial Constraint-Based Clustering and Fine Tuning

JING XIA [1], (Associate Member, IEEE), XUEMEI LI [1], GUONING CHEN [2], AND CAIMING ZHANG [1]

[1] School of Computer Science and Technology, Shandong University, Jinan 250101, China
[2] Department of Computer Science, University of Houston, Houston, TX 77204, USA

Corresponding author: Caiming Zhang (czhang@sdu.edu.cn)

This work was supported in part by the NSFC Joint Fund with Zhejiang Integration of Informatization and Industrialization under Key Project under Grant U1609218, and in part by the Natural Science Foundation of Shandong Province under Grant ZR2017MF033 and Grant ZR2018BF009.

ABSTRACT Tissue segmentation from a single brain MR image is of paramount importance for brain reconstruction and analysis. In this paper, we propose a new hybrid algorithm for brain MR image segmentation, combining super-resolution, spatial constraint based clustering and fine-tuning. To smooth noise and improve image clarity, we first amplify the brain MR image by using a super-resolution algorithm – cubic surface fitting with edges in the image as constraints. Then an improved fuzzy c-means clustering algorithm is performed on the amplified image for the global segmentation, in which a shape parameter and an anomaly detection parameter are introduced. With the introduction of these two parameters, the robustness of the clustering is enhanced, and the trade-off between noise smoothing and detail preservation can be controlled more accurately. Furthermore, the local regions around boundaries of different brain tissues (e.g., gray matter (GM), white matter (WM) and cerebrospinal fluid (CSF)) are re-segmented in a fine-tuning process, and a soft voting strategy is adopted for adjusting the incorrect pixels, which makes full use of the boundary details of different tissues. Experimental results show the new algorithm can preserve major brain tissue structures and smooth out noise.

INDEX TERMS Fuzzy c-means, coefficient of variation of local window, shape parameter, fine-tuning.

I. INTRODUCTION

Image segmentation is one of the most important techniques in image understanding and computer vision, and applied in many fields, such as objection detection, medical imaging analysis, etc. Segmentation is to partition one image into homogeneous and non-overlapping regions with respect to certain characteristics, such as intensity, texture and shape [1]. Magnetic Resonance (MR) imaging has several advantages over other medical imaging modalities, including the high contrast between different soft tissues, relatively high spatial resolution across the entire field of view and multi-spectral characteristics. Accurate segmentation of brain MR images according to tissue types (e.g., gray matter (GM), white matter (WM) and cerebrospinal fluid (CSF)) or relevant anatomical structures (e.g., cortex, ventricles, hippocampus, etc.) is often the first step to extract features, which are useful for the identification of disease-specific morphological differences [2]. The major obstacles for brain MR image segmentation are partial volume effect (PVE), intensity inhomogeneity (IIH) [3] and noise [4]. In recent years, many works on brain MR image segmentation have been proposed, such as segmentation based normal cut, graph cut, geodesic distance, mean shift and random walk [5].

In the brain MR images, due to the partial volume effect, it is difficult to assign the effected pixels to one single tissue. In this case, the conventional hard segmentation methods are not the first choice to segment brain MR images [3], because each pixel is restricted to one class exclusively in these methods. Different from the hard segmentation methods, fuzzy clustering allows one pixel to belong to multiple classes concurrently, which considers the ambiguity in clustering and

The associate editor coordinating the review of this manuscript and approving it for publication was Jenny Mahoney.

retains more information than hard segmentation methods. Therefore, it is more widely applied in brain MR image segmentation. Fuzzy c-means, abbreviated as FCM, is one representative fuzzy clustering method, and is widely applied in medical image segmentation. FCM performs well in noise-free images, while poorly in images effected by noise, outliers or other images artifacts [6]. This is because spatial information is not considered in its objective function. Aiming to overcome this problem, several improved algorithms have been proposed to improve the conventional FCM mainly by updating the membership parameter [7], [8], objective function Miao *et al.* [9], Zhang *et al.* [10], Kumar *et al.* [11].

Due to the effect of noise, the boundary in the original brain MR image is not clear enough, especially the boundary between gray matter and cerebrospinal fluid. Moreover, the partial volume effect causes small difference between different tissues near the boundary, especially between the gray matter and the white matter. Considering these issues, those improved algorithms still have some problems as follows: (1) They do not enhance the clarity of the input image. (2) The estimation of influence from the neighboring pixels to the central pixel in the brain MR image is not accurate enough. (3) The local information including boundary details is not utilized. To improve the segmentation results, we propose a new algorithm for brain MR image segmentation, which combines super-resolution, spatial constraint based clustering and fine-tuning, defined as Spatial constraint based FCM with Fine-Tuning (denoted as SFCMFT). First, we use a super-resolution algorithm to pre-process the input brain MR image, aiming to smooth out noise while improving image clarity. After this pre-processing, the boundaries of different tissues are enhanced. Then, an improved fuzzy c-means clustering algorithm is performed on the amplified image to obtain the initial segmentation, in which a shape parameter and an anomaly detection parameter are introduced. With the introduction of these two factors, the robustness of the segmentation can be enhanced and the trade-off between noise removal and detail preservation can be controlled more accurately. Furthermore, the local regions around boundaries of different tissues are re-segmented in a fine-tuning process, and a soft voting strategy is adopted for adjusting the incorrect pixels. This process makes full use of the boundary details between different tissues. Our new algorithm is noise-tolerant and can generate accurate segmentation results robustly.

In general, our contributions include three aspects. (1) We propose a new global segmentation algorithm by defining a shape parameter and an anomaly detection parameter, which not only consider the influences of neighbors, but also judge if the neighbors are noise pixels. In this case, the influences of noise pixels will be reduced, while the influences of the clean pixels will be increased automatically. (2) We propose the fine-tuning step to refine the pixels near boundaries more accurately. (3) We propose a general framework of combining super-resolution, global segmentation and fine-tuning steps, to achieve more accurate segmentation results. Our framework is also suitable for other clustering algorithms and applications.

II. LITERATURE REVIEW

Ahmed proposed FCM_S algorithm [12] by introducing neighboring pixels into the objective function. Chuang *et al.* proposed an improved FCM (SAFCMpq) [13] algorithm that defines a spatial function, which is used to update the membership value of each pixel after taking its neighboring pixels membership values into account. Moreover, considering that the number of the pixels is larger than the number of the gray levels (ranging from 0 to 256) in grey-scale image, especially in brain MR images, Zhang *et al.* [14] utilized the gray histogram of the image instead of pixels for clustering. Szilagyi *et al.* [15] developed an enhanced FCM (EnFCM) algorithm to accelerate the clustering process, and the computational time of the algorithm was reduced greatly. Furthermore, Cai *et al.* [16] proposed the fast generalized FCM (FGFCM) algorithm. This method introduces a local similarity metric that combines both spatial and gray level information to form a non-linearly weighted sum image. By adopting the technique of EnFCM, FGFCM can be computed efficiently.

Although the algorithms mentioned above enhance the robustness to noise effectively, they need to select proper parameters to achieve a desired trade-off between robustness to noise and the preservation of details. Generally speaking, the selection of these parameters has to be made empirically or via trial and error. To solve this problem, Stelios and Vassilios [17] introduced a fuzzy local information c-means (FLICM) by incorporating the local spatial information and gray level information into the clustering. This algorithm is free of the empirically adjusted parameters. In consideration of both the spatial distance and the gray-level difference among neighboring pixels, Gong *et al.* designed a new trade-off weighted fuzzy factor to measure the damping extent. By introducing this new fuzzy factor into FCM algorithm, they proposed an improved FLICM algorithm. It introduces a kernel metric to enhance the robustness to noise, which is denoted as KWFLICM [18]. Above algorithms could balance the weight between removing noise and remaining the details in image automatically, by introducing the spatial information. However, due to these methods don't consider the preprocessing of brain MR images, the segmentation results can be improved further. References [19], [20] proposed to preprocess the MR images by using the simple linear iterative clustering (SLIC) algorithm, which is a superpixel dividing method and can generate superpixels by combining the pixels with similar gray values in the image. Because SLIC is a kind of down-sampling methods, some detail information of the MR image will lost. Sarkar and Halder introduced the rough theory into fuzzy c-means clustering, and they proposed novel rough-fuzzy c-means algorithms, which could adjust the weight to control the effect of rough factor automatically [2], [8].

However, the performance of only combining rough theory is still limited.

III. BASIC IDEA

For brain MR image segmentation, getting the right and accurate brain tissues depends on two key factors. One is that the brain MR image is clear. It means that the boundaries and the junctions of different brain tissues are clearly distinguishable and the effect of noise is small. The other is a robust segmentation algorithm. Considering these two key factors, we propose a new hybrid segmentation algorithm that consists of an image super-resolution pre-processing, a spatial constraint based clustering and a fine-tuning process. In the following, we first state the basic ideas of these three steps.

A. BASIC IDEA OF IMAGE SUPER-RESOLUTION

The noises in the input image are expected to be reduced, while the details and boundaries are expected to be preserved by using a good super-resolution algorithm, which is vital for the subsequent segmentation [19]. To enhance the clarity of the boundaries of brain tissues while smoothing out the noise in image, we select a cubic surface fitting super-resolution to amplify the given brain MR images.

B. BASIC IDEA OF SPATIAL CONSTRAINT BASED CLUSTERING

After super-resolution pre-processing, we obtain brain MR images with higher resolution and less noise. A good segmentation method is then needed, which can resist a small amount of noise while preserve the boundaries of brain tissues as much as possible. In FLICM, a novel fuzzy factor is defined to encode the neighbor information, which uses the distance from the neighboring pixels to the center pixel to measure the influence of the neighboring pixels automatically. However, this fuzzy factor in FLICM cannot reflect the accurate neighboring information sometimes. Our new algorithm replaces this fuzzy factor with a shape parameter and an anomaly detection parameter. The shape parameter uses a variation coefficient, aiming to reflect the different effects of neighbors in different local windows that may be impacted by different levels of noise. It can measure the influence of the neighboring pixels on the center pixel more accurately. Thus, we can get more accurate weight to balance noise removal and detail preservation. The anomaly detection parameter checks and corrects the error effects from the neighboring pixels, which are caused by either noise or boundaries of different tissues. In short, the new global segmentation can determine the weight based on the influence of the neighboring pixels on their center pixels automatically, and achieve a more desired trade-off between noise removal and detail preservation.

C. BASIC IDEA OF FINE-TUNING

The result of the global segmentation is generally acceptable, and the incorrect segmentation mainly concentrates near the boundaries of brain tissues. For brain MR image, due to the noise and partial volume effect, the values of pixels in the same tissue are not exactly same. In that case, the differences of the gray values of pixels in the same tissue could be even larger than the differences across different tissues, especially near the junctions of two or more tissues. Since the segmentation is based on the gray values of pixels, it may incorrectly assign the pixels in different tissues into the same class, or assign the pixels in the same tissues into different classes, resulting in incorrect tissue boundaries.

To overcome this problem, we propose a fine-tuning process to make a better use of the local information near the boundaries, and re-segment the boundary regions in the result of the global segmentation. After this re-segmentation, we correct the pixels distributed in the wrong class, and fine-tune the boundary. Because the number of pixels in each local region near boundary is less than the whole image, the differences of pixel values in the same tissue in the local region is less too. Hence, this local re-segmentation can be performed more accurately than the above global segmentation.

The rest of this paper is organized as follows. In Section IV, we describe our super-resolution process. In Section V we introduce the global segmentation algorithm in details. In Sections VI and VII, we introduce the fine-tuning and merging process, and then we present experimental results on various brain MR images in Section VIII. Finally, we summarize the paper in Section IX.

IV. IMAGE SUPER-RESOLUTION PRE-PROCESSING

As discussed earlier, an effective super-resolution, which can both suppress noise in image and preserve details of brain tissue boundaries, is needed to pre-process the input image. To identify the most suitable algorithm, we have tested a large number of super-resolution methods on brain MR images with noise, including the cubic surface fitting algorithm [21], Yang *et al.*'s algorithm [22], GR algorithm [23] and NE+LLE algorithm [24], as shown in FIGURE 1. The input image is from BrainWeb, an open simulation brain dataset online, and the noise level of it is 9% (from 0 to 9%, 0 means no noise, higher percentage means heavier noise). The gray value distribution of the noise in the simulation image follows a Gaussian density function, whose average value is 0. The standard deviation of this Gaussian density function is the product of the noise level and the average of the gray value of the white matter. In FIGURE 1(c), the amplified result by using Yang *et al.*'s algorithm is obviously fuzzier than the others visually.

To compare these algorithms quantificationally, we compute the error image, which is a difference map between the amplified result and the clear image. The value of each pixel in the error image indicates the gray value difference between the corresponding pixels in amplified image and the clear image, respectively. Here, the clear image is the corresponding input image with 0 noise in BrainWeb. Note that, to make the resolution of the amplified image identical

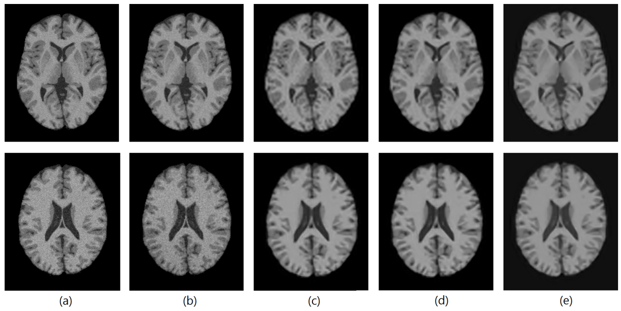

FIGURE 1. **The image super-resolution results of different cross sections of the brain images: (a) input image, (b) cubic surface fitting, (c) Yang *et al.*, (d) GR (e) NE+LLE.**

to the resolution of the clear image, we first down sample the input image, and then amplify the downsampled image using these algorithms. FIGURE 2 shows the error line charts of the error images of the amplified results in the first row of FIGURE 1. The X and Y axes correspond to the gray value difference and the number of pixels, respectively. Intuitively, the fewer the pixels have large gray value difference, the better the super-resolution algorithm performs. The error line chart of the input noise image is shown as the orange curve, and the error line charts of the amplified images by using the improved cubic surface fitting algorithm, Yang *et al.*'s algorithm, GR algorithm and NE+LLE algorithm are shown as red, blue, pink and green curves respectively. From the plots, we can see that the improved cubic surface fitting algorithm (i.e., the red curve) has the best accuracy among the tested algorithms. This is likely because it takes both the continuity and smoothness conditions into account. Hence, we select this algorithm for our image super-resolution pre-processing.

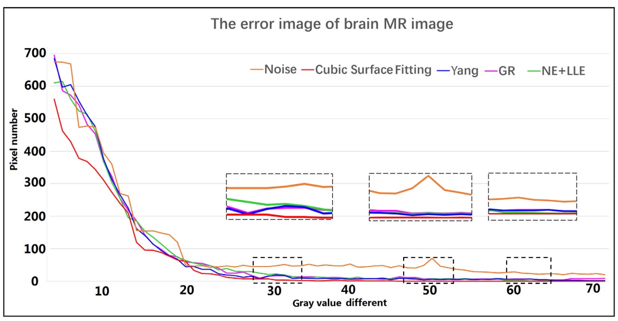

FIGURE 2. **The line chart of the error images shown in FIGURE 1.**

To illustrate that the improved cubic surface fitting algorithm could better preserve boundaries, we take the local windows containing certain boundaries cut from the amplified images as examples. These local windows and their corresponding error images are shown in FIGURE 3, and the mean error values and PSNR (peak signal-to-noise ratio) are shown in TABLE 1. Compared to the results of other algorithms, the improved cubic surface fitting algorithm apparently preserves more boundary information, and its mean error value is the smallest while its PSNR is the highest.

TABLE 1. **Mean error values of error images and PSNR by using different amplified methods on FIGURE 1.**

Amplified methods	Noise image	Cubic surface fitting	Yang et al.	GR	NE+LLE
Mean errors	13.371	4.317	9.735	11.286	6.492
PSNRS	75.593	87.413	80.350	79.066	82.625

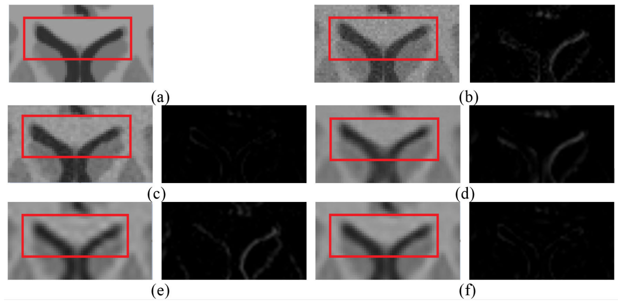

FIGURE 3. **The boundary of the super-resolution results: (a) the clear image, (b) the error image of noise image, (c) the error image of the improved cubic surface fitting algorithm, (d) the error image of Yang *et al.*'s algorithm, (e) the error image of GR algorithm, (f) the error image of NE+LLE algorithm.**

Nonetheless, the improved cubic surface fitting algorithm only filters out the high-frequency noise. The amplified image still contains noise, which requires a robust global segmentation algorithm to handle it.

V. IMAGE CLUSTERING

To enhance the robustness to noise, FLICM introduces a novel fuzzy factor that uses the spatial distance information from the neighboring pixels to their center pixel to measure the trade-off between noise removal and detail preservation. However, spatial distance information is not enough to measure the trade-off in the real-world scenarios. To address this, KWFLICM further introduces a trade-off weighted fuzzy factor that is computed based on the difference between a variation coefficient of the direct neighborhood of the central pixel, and an average variation coefficient within a local window. Ideally, when the pixels within the local window are effected by noise more heavily, the trade-off weight should be larger in order to smooth out noise. However, when the local window is effected by noise very heavily, both the variation coefficient of the neighborhood and the average variation coefficient within the local window might be large. In this case, the difference of these two large values might be small oppositely, leading to smaller trade-off weight. This is contrary to our expectation.

Both KWFLICM and FLICM can measure the effect of the neighbors to the center pixel automatically to some extent, but they still cannot produce ideal results when the configuration of the noise is complex. FIGURE 4 provides an example of such a complex configuration, and the brain MR image is from BrainWeb. The noise level of FIGURE 4(a) is 7%.

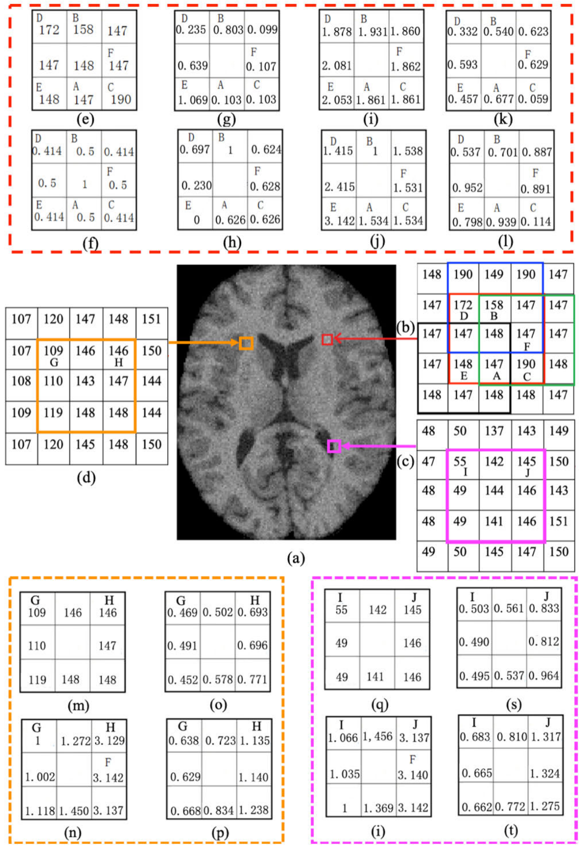

FIGURE 4. The comparison of fuzzy factors from KWFLICM with those computed by using our method. (a) the noise image, (b)-(d) gray values of three windows extracted from (a). Specifically, (c) and (d) cover the boundaries of WM and CSF, WM and GM, respectively. (e)-(l) are the fuzzy factors in (b). Specifically, (e) gray value of central window in (b), (f) local spatial constraint in FLICM, (g) $|C_j - \bar{C}|$ in KWFLICM, (h) $\frac{C_j - C_{min}}{C_{max} - C_{min}}$ in our algorithm, (i) fuzzy factor in KWFLICM, (j) shape parameter, (k) anomaly detection parameter, (l) τ_{cr}. (m)-(q) and (q)-(t) are the fuzzy factors in (d) and (c), respectively. Specifically, (m) and (q) gray values of central windows in (d) and (c), (n) and (r) shape parameters in (m) and (q), (o) and (s) anomaly detection parameters in (m) and (q), (p) and (t) τ_{cr}s in (m) and (q).

A 5 × 5 window is extracted from the noise brain MR image (marked by a red rectangle in FIGURE 4(a)), and the gray value of this window is shown in FIGURE 4(b). In the local window marked by the red rectangle in FIGURE 4(b), compared to the corresponding clear image (noise level is 0) in BrainWeb, the central pixel is identical to the original value, and its three neighbors B, C, D are effected by noise to varying degrees.

Under the above configuration, the fuzzy factor value based on KWFLICM is shown in FIGURE 4(i). From this result, we can see when a pixel is noise, like pixel B or D, its effect to the center pixel is large. On the contrary, when a pixel is noiseless, like pixel A or E, its effect is small. This will make the noiseless pixels to be disturbed by its neighboring noise pixels, which is contrary to our expectation. This example shows that KWFLICM cannot properly determine the weight to balance noise removal and detail preservation when the configuration of the noise is complex.

A. THE SHAPE PARAMETER

In FIGURE 4(b), compared to the corresponding clear image, there are four noise pixels in the local window centered at B (marked by a blue rectangle), and their gray values are 190, 190, 158 and 172, respectively. In the meantime, there are two noise pixels B and C in the local window centered at F (marked by a green rectangle), whose gray values are 158, 190, respectively. The coefficient of variation at the center pixel u (e.g., pixels B and F in the above example) is defined as follows:

$$C_u = \frac{R_{v,a}(x)}{(\bar{x})}, \tag{1}$$

where $R_{v,a}$ and $\bar{x}$ represent the intensity variance and mean in a local window of the image, respectively.

The value of C_u reflects gray value homogeneity degree of the local window. It exhibits high value at edges or in the area corrupted by noise and produces low value in homogeneous regions. In the local window marked by a red rectangle in FIGURE 4(b), the maximum and minimum coefficients of variation are $C_B = 1.874$ and $C_E = 0.0017$, respectively, and the average coefficient of variation within this local window is $\bar{C} = 1.071$. In KWFLICM, the fuzzy factor uses $|C_j - \overline{C}|$ to measure the influence from neighboring pixels, as shown in FIGURE 4(g). Since this local window is heavily effected by noise, the average of coefficient of variation is high too. This situation causes a low difference value between C_B and $\bar{C}$, even lower than the difference between C_E and $\bar{C}$, which cannot accurately reflect the influence of noise.

In order to avoid the error caused by the above average coefficient of variation, we normalize the variation coefficient by the difference between the maximum and the minimum coefficients of variation, so that it ranges from 0 to 1. The new variation coefficient is then defined as follows:

$$\xi_j = \frac{C_j - C_{\min}}{C_{\max} - C_{\min}}, \tag{2}$$

$C_{\min}$ and $C_{\max}$ are the minimum and maximum coefficients of variation, respectively.

The new variation coefficients in the above local window are shown in FIGURE 4(h). As can be seen, the new coefficient of pixel B is close to 1, whose local neighborhood (marked by the blue rectangle) has a large coefficient of variation. In the meantime, the new coefficient of pixel E is close to 0, whose neighborhood (marked by the black rectangle) has a small coefficient of variation. This indicates the new coefficient accurately reflect the influence of noise. The coefficient of variation could reflect the complexity of shapes in the local window to some extent. We define a shape parameter by using the coefficient of variation, which could measure the influences from neighbors to central pixel automatically. When the coefficient of variation is higher, the shapes in the local window are more complicated, and the influences from neighbors to central pixel should be smaller. Oppositely, when the coefficient of variation is lower, the shapes in the local window are simpler, and the influences from neighbors to central pixel should be larger. In the meantime, it is expected when the variation coefficient is close to 1, the shape parameter should decline quickly; and when the variable coefficient is close to 0, the shape parameter should increase quickly. To satisfy this relationship, we define the shape parameter as follows:

$$\delta_{sc} = \pi^{(1-\xi_j)}, \tag{3}$$

δ_{sc} is the shape parameter, ranging from 1 to π. δ_{sc} and ξ_j have an inverse correlation. When ξ_j is close to 0, δ_{sc} is close to π, and when ξ_j is close to 1, δ_{sc} is close to 1 according to equation (3), as shown in FIGURE 5. In other words, when the window is effected by noise heavily or around the boundaries, ξ_j is close to 1 and δ_{sc} is close to 1, which will reduce the effects of neighbors. When the window is smooth, ξ_j is close to 0 and δ_{sc} is close to π, which will increase the effects of neighbors. The shape parameter from equation (3) is shown in FIGURE 4(j). Compared to the fuzzy factor of KWFLICM shown in FIGURE 4(i), the new shape parameters of pixels E and F are higher, while the shape parameters of B and D are lower. It means the new shape parameter can measure the effect of noise more accurately.

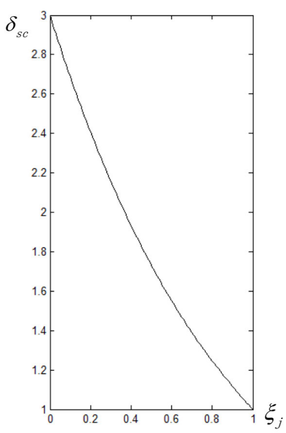

FIGURE 5. The change of δ_{sc} with ξ_j.

B. THE ANOMALY DETECTION PARAMETER

The design of δ_{sc} did not included the case that the neighboring pixels are anomaly in the current FCM. In FIGURE 4(b), there is a noise pixel whose gray value is 190 in windows centered at neighboring pixels C and A, respectively. The shape parameter of the window centered at A is as same as the shape parameter of the one centered at C, as shown in FIGURE 4(h). However, since the neighboring pixel C is effected by noise, the influence of the neighboring pixel C to the central pixel should be smaller than the influence of the neighboring pixel A.

To solve the above problem, we introduce an anomaly detection parameter to face the case that a neighbor is noise or boundary pixel. The larger the gray value of the neighboring pixel is different from the average gray value of the window, the more likely the neighbor is a noise pixel or on the boundary, and thus the smaller impact of the neighboring pixel should have on the central pixel. On the contrary, the less the gray value of neighbor is different from the average of gray value of the window, the less likely the neighbor is a noise pixel, and the greater impact of the neighboring pixel should have on the central pixel. Therefore, we define the anomaly detection parameter by using the difference of the gray values between neighboring pixels and the central pixel. To measure the difference relatively, we use the z-score to define the anomaly detection parameter. Z-score measures how many standard deviations below or above the mean of the gray value of the window. The anomaly detection parameter is then defined as follows:

$$\delta_{sr} = e^{-\frac{|x_j - \bar{x}|}{Sd(x_j)}}, \tag{4}$$

x_j is the gray value of a neighboring pixel j. $\bar{x}$ is the average gray value of the local window centered at x_j. $Sd(x_j)$ is the standard deviation of the local window, and $\frac{|x_j-\bar{x}|}{Sd(x_j)}$ is the z-score. δ_{sr} is the anomaly detection parameter, ranging from 0 to 1. The lower value of z-score is, the less difference of the gray values between the neighboring pixel and the central pixel is, and the less possibility the neighboring pixel is a noise pixel. In this case, the value of δ_{sr} is high, and the impact of neighboring pixel on the central pixel is large. On the contrary, the higher the value of z-score is, the larger difference of the gray values between the neighboring pixel and the central pixel is, and the more possibility the neighboring pixel is a noise pixel. In this case, the value of δ_{sr} is low, and the impact of neighboring pixels on the central pixel is small. According to equation (4), we obtain that the value of the anomaly detection parameter of pixel C is lower than A, which means C is more likely to be a noise pixel than A, as shown in FIGURE 4(k).

C. THE NEW FUZZY FACTOR

We define a new fuzzy factor by combining the above shape parameter and the anomaly detection parameter. When the value of shape parameter δ_{sc} is high, the neighboring pixels in a window are effected by noise slightly or not on the boundary. In this situation, we can use anomaly detection parameter δ_{sr} to compute the probability of a neighboring pixel being noise or on boundary. When δ_{sr} is high, the neighbor is more likely to be a noiseless pixel or not on boundary, and the influence of the neighbor on central pixel is large. On the contrary, when δ_{sr} is low, the neighbor is more likely to be a noise pixel or on the boundary, and the influence of the neighbor on the central pixel is small. When the value of shape parameter δ_{sc} is small, the window is effected by noise heavily, or the window is around the boundary. In this case, due to the large changes of gray scale values within the local window, and the central pixel may be noised, we cannot get the probability of the neighbors being noise from δ_{sr}. To avoid the influence of noise on the noiseless pixel, the effect of neighbors on the central pixel should be as less as possible. In short, when δ_{sc} and δ_{sr} are both high, the influence of neighbors on central pixel should be high; otherwise, the influence of neighbors on the central pixel should be low. To achieve this goal, the relationship of δ_{sc} and δ_{sr} is defined as the harmonic mean as the following:

$$\tau_{cr} = \frac{2 \times \delta_{sc}.\delta_{sr}}{\delta_{sc} + \delta_{sr}}, \tag{5}$$

τ_{cr} ranges from 0 to $\frac{2\pi}{\pi+1}$. The harmonic mean can assure only when the values of δ_{sc} and δ_{sr} are both high, the value of τ_{cr} is high. Compared to FLICM and KWFLICM, all the values of τ_{cr} of the noiseless pixels A, E and F are higher than those of the noise pixels B, C, and D, as shown in FIGURE 4(l).

We also compare our definition with the ones using the quadratic mean $\tau_{cr} = \frac{{\delta_{sc}}^2+{\delta_{sr}}^2}{2}$, geometrical mean $\tau_{cr} = \sqrt{\delta_{sc}.\delta_{sr}}$ and arithmetic mean $\tau_{cr} = \frac{\delta_{sc}+\delta_{sr}}{2}$, respectively. The resultant fuzzy factors of the example (FIGURE 4(b)) computed by the four average methods are shown in FIGURE 6. Since arithmetic mean and quadratic mean are easily effected by the extreme data, pixel C is noised but it has a high fuzzy factor, which is unreasonable. The geometrical mean can reduce the effect of the extreme numerical value, but cannot get low value when one of δ_{sc} and δ_{sr} is low, (e.g., the fuzzy factor value of pixel C). Only the harmonic mean can assure when the values of δ_{sc} and δ_{sr} are both high, the value of τ_{cr} is high.

D 0.537	B 0.701	0.887
0.952		F 0.891
E 0.798	A 0.939	C 0.114

(a)

D 1.056	B 0.646	1.377
3.092		F 1.370
E 5.039	A 1.406	C 1.179

(b)

D 0.685	B 0.735	0.979
1.197		F 0.981
E 1.198	A 1.019	C 0.301

(c)

D 0.873	B 0.770	1.081
1.504		F 1.080
E 1.799	A 1.105	C 0.797

(d)

FIGURE 6. Results of the fuzzy factors of FIGURE 4(b) computed by the four average methods: (a) Harmonic mean $\tau_{cr} = \frac{2\times\delta_{sc}.\delta_{sr}}{\delta_{sc}+\delta_{sr}}$, (b) quadratic mean $\tau_{cr} = \frac{{\delta_{sc}}^2+{\delta_{sr}}^2}{2}$, (c) geometrical mean $\tau_{cr} = \sqrt{\delta_{sc}.\delta_{sr}}$, (d) arithmetic mean $\tau_{cr} = \frac{\delta_{sc}+\delta_{sr}}{2}$.

To further evaluate the efficacy of our proposed shape parameters and anomaly detection parameters, we also present the parameters regarding another configuration that covers two types of tissues (WM and CSF, WM and GM), as shown in FIGURE 4 (c) and (d). Specifically, (c) and (d) are two 5×5 windows covering the boundaries between WM and CSF, WM and GM, respectively, extracted from the brain MR image (marked by pink and orange rectangles in FIGURE 4(a)). The gray values, shape parameters, anomaly detection parameters and τ_{cr}s of these two windows are shown in FIGURE 4(q)-(t) and (m)-(p), respectively. The parameters are large when the gray values of neighboring pixels are more similar to the gray values of centers, which means the neighbors and centers might belong to the same cluster (e.g., pixels H in (d) and J in (c)). On the contrary, the fuzzy factors are small when the gray values of neighboring pixels are less similar to the gray values of centers, which means the neighbors and centers might belong to different clusters (e.g., pixels G in (d) and I in (c)).

Combining the spatial distance function in FLICM, the new fuzzy factor is defined as follows:

$$\delta_{ij} = \delta_{sd}.\tau_{cr}, \tag{6}$$

and

$$\delta_{sd} = \frac{1}{d_{ij}+1}. \tag{7}$$

δ_{sd} is a local spatial constraint, same with that in FLICM (as shown in FIGURE 4(f)), and d_{ij} is the distance between the pixel i and pixel j. The trade-off weighted fuzzy factor is defined as:

$$G'_{ki} = \sum_{j\in N_i} \delta_{ij}(1-\mu_{kj})^m ||x_j - v_k||^2. \tag{8}$$

Here, j is a neighbor of pixel i. μ_{kj} is the membership of the pixel j belonging to the cluster k. v_k is the cluster center of the cluster k. $m \geq 1$ is a parameter to control the fuzziness of the clustering results. The effect and set of m are discussed in [25]. Here, m is set as 2 according to experience.

D. GLOBAL SEGMENTATION

The energy function of the improved global segmentation is defined as:

$$E = \sum_{i=1}^{N}\sum_{k=1}^{C}(\mu_{ki}^m||x_i - v_k||^2 + G'_{ki}). \tag{9}$$

Here, N is the number of pixels in the given image, and C is the predefined number of clusters. In our paper, C is set as 4. The new membership update function and clustering center update function are as follows:

$$\mu_{ki} = \frac{1}{\sum_{l=1}^{C}\left(\frac{||x_i-v_k||^2+\sum_{i=1}^{N}\sum_{j\in N_i}\delta_{ij}(1-\mu_{kj})^m||x_j-v_k||^2}{||x_i-v_l||^2+\sum_{i=1}^{N}\sum_{j\in N_i}\delta_{ij}(1-\mu_{lj})^m||x_j-v_l||^2}\right)^{1/(m-1)}}, \tag{10}$$

$$v_k = \frac{\sum_{i=1}^{N}\mu_{ki}^m x_i + \sum_{i=1}^{N}\sum_{j\in N_i}\delta_{ij}(1-\mu_{kj})^m {x_j}^2}{\sum_{i=1}^{N}\mu_{ki}^m + \sum_{i=1}^{N}\sum_{j\in N_i}\delta_{ij}(1-\mu_{kj})^m}. \tag{11}$$

The framework of global segmentation is illustrated in Algorithm 1.

The improved global segmentation can estimate the influence of the neighboring pixels on the center pixel accurately. Compared to other FCM algorithms, our improved algorithm can produce more precise boundary, as shown in FIGURE 7. Note that, the input image in FIGURE 7 is the amplified image after super-resolution process. The first row shows the segmentation result, and the second and third rows are the magnified views for the regions enclosed by these two green rectangles. To quantitatively evaluate the global segmentation results, we present the dice similarity coefficient (DSC, defined in result section) results of FIGURE 7, as shown in TABLE 2. Compared with the other three algorithms,

Algorithm 1 The Global Segmentation

Input: image I; the number of pixels N; the number of clusters C; the max iteration T; threshold e;
Output: membership matrix $U = \{\mu_{11}, \mu_{21}, .., \mu_{k1}, \ldots, \mu_{ki}, \ldots\}$; cluster center $V = \{v_1, v_2, .., v_k\}$;
Initialize partition U randomly;
for $t = 1$ to T **do**
  for $i = 1$ to N **do**
    for $k = 1$ to C **do**
      update the cluster center v_k by using equation (11);
      update the membership μ_{ki} by using equation (10);
    end for
  end for
  calculate the new objective function E_t by using equation (9);
  if $abs(E_t - E_{t-1}) < e$ **then**
    break;
  else
    $E_{t-1} = E_t$;
  end if
end for

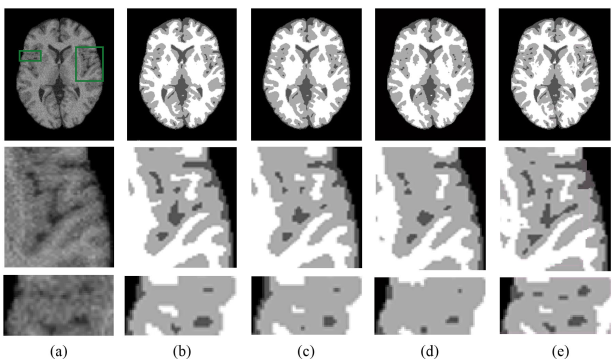

FIGURE 7. The results of the global segmentation. The first row shows the segmentation results, and the second and third rows are the magnified views for the regions enclosed by these two green rectangles. (a) input image, (b) FCM_S, (c) FLICM, (d) KWFLICM, (e) the global segmentation.

TABLE 2. The dice similarity coefficient (DSC) for FIGURE 7.

Input image	FCM_S	FLCIM	KWFLICM	The global segmentation
Fig. 7	0.873	0.885	0.895	0.916

the global segmentation can get higher DSC, meaning that it performs better than other algorithms.

VI. FINE-TUNING PROCESS

A. THE DEFINITION OF DETECTION WINDOW

Compared to other FCM algorithms, our global segmentation can obtain more accurate boundary, for example, the boundary between the gray matter and the cerebrospinal fluid, as shown in the green rectangles in FIGURE 7. Since the utilization of image details is lack, as introduced in Section III, the result is still not accurate enough, especially on the boundary between the white matter and gray matter, as shown in the magnified views in FIGURE 7(e).

Considering that the inaccurate results are typically reflected in the wrong classification of pixels on boudaries, SFCMFT algorithm makes the best use of boundary information and re-segments the regions around boundaries, to improve the accuracy of the segmentation and enhance the robustness. To achieve this goal, we define a square window with $r \times r$ pixels. In the fine-tuning process, we move the window along the boundary from top to bottom and left to right without being crossed, at the rate of one pixel per move. FIGURE 8 shows the sliding process on a local picture cut from the image result of global segmentation, in which r is set as 6. As shown in FIGURE 8, the tissue boundary of the global segmentation is marked by red lines, and the sliding orientations are marked by the yellow arrows. When we move the window to the pixel i, we can get a detection window centered at pixel i, denoted as D_i, marked by the black rectangle in FIGURE 8.

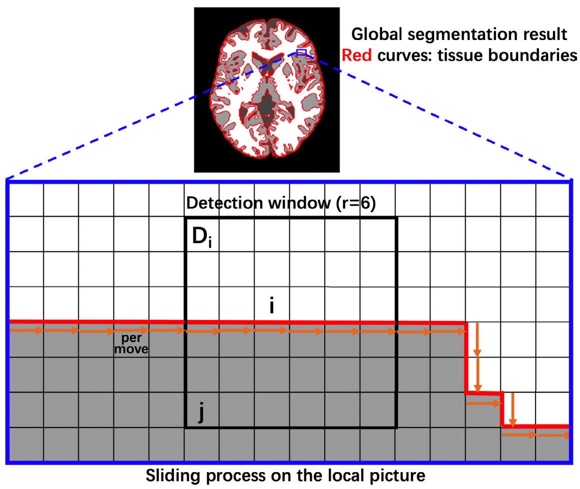

FIGURE 8. The sliding process shown on a local image of the global segmentation result. Top image: global segmentation result, the red curves represent the tissue boundary. Bottom image: sliding process on a local image cut out from the top image. The boundary is marked by red line, and the sliding orientations are marked by the orange arrows. The detection windows are marked by the black rectangle.

B. LOCAL FINE-TUNING PROCESS

To refine the detailed features around the boundary and optimize the boundary, we re-segment the regions within the detection windows and correct the boundary pixels.

FIGURE 9(b)-(d) are brain MR image segmentation results by using FLICM, KWFLICM and our global segmentation method, respectively, and (g)-(j) are the local windows amplified by 30 times. Red curves in FIGURE 9(e) mark the boundaries of our global segmentation result. FIGURE 9(f) is a local window containing imprecise boundaries (marked by black lines). Compared to the ground truth shown in

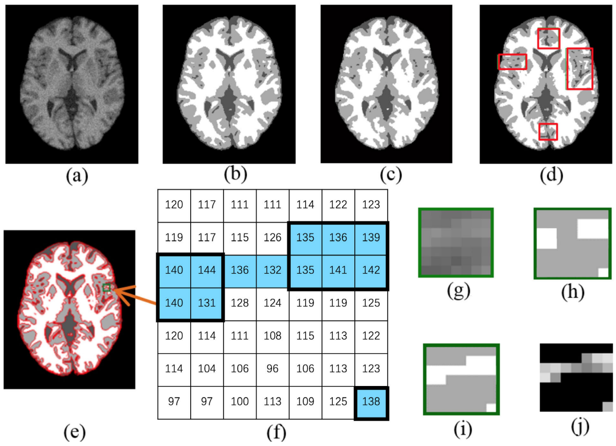

FIGURE 9. The re-segmentation utilizing the local information of the detection window: (a) input image, (b) FLICM, (c) KWFLICM, (d) global segmentation, (e) boundaries of (d), (f) gray value of local window, (g) local window from (a), (h) result from (d), (i) local segmentation result, (j) ground truth.

FIGURE 9(j), the pixels whose gray values are above 130 should be in the same cluster in FIGURE 9(f) (marked by blue color). FIGURE 9(i) shows the local segmentation result achieved by re-applying our global segmentation method on FIGURE 9(g), and it is closer to the ground truth. So the effective utilization of the local information plays an important role to improve the accuracy.

The number of classes in the detection window is determined by the result of the global segmentation. If the number of classes in the detection window after the global segmentation is c', the number of classes in the detection window is supposed to be c' in re-segmentation.

C. VOTING STRATEGY

Because the window is slid along the boundary at the rate of one pixel per move, some pixels are overlapped in the adjacent detection windows. These overlapped pixels might be distributed to different clusters in the re-segmentation results of these adjacent detection windows. For each overlapped pixel j, we retune its cluster by majority vote. Specifically, for each cluster k, $V_k(i)$ represents the "vote" from the detection window D_i containing the pixel j, which represents the possibility that pixel j is distributed to the cluster k in the detection window D_i. Then, we compute the total votes that this cluster received by summing the votes $V_k(i)$ from all detection windows D_i containing pixel j. Finally, the pixel j is distributed to the cluster with the maximum total votes.

Here, we introduce two voting strategies to define $V_k(i)$. The simplest strategy is setting $V_k(i)$ as 1 (or 0), when the pixel j is (or is not) distributed to the cluster k in the detection window D_i after re-segmentation. In this way, the pixel j is only distributed to one cluster in each detection window, so it is called hard voting strategy. On the contrary, assuming pixel j could be distributed to more than one cluster in each detection window, the second one is soft voting strategy. In the soft voting strategy, $V_k(i)$ is defined as the membership of the pixel j to the cluster k in the detection window D_i after re-segmentation. The fine-tuning results of two voting strategies are shown in FIGURE 10. Due to the soft voting strategy considering the membership between pixel and cluster, it can reflect more image information and get more accurate segmentation results, as shown in the red rectangle in FIGURE 10. Therefore, we adopt the soft voting strategy in the fine-tuning process.

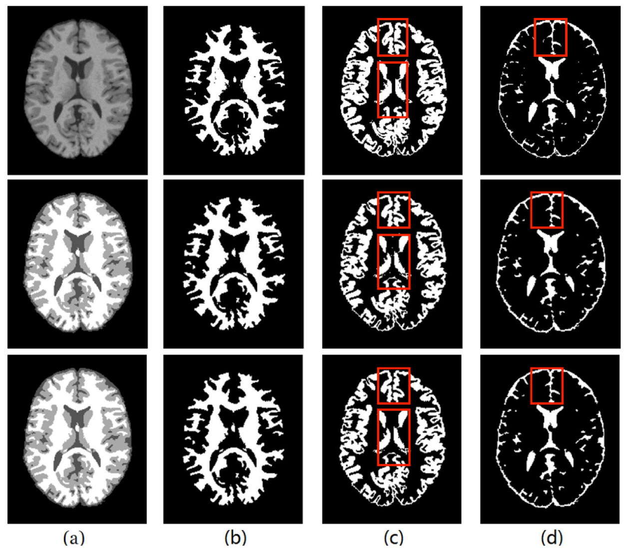

FIGURE 10. The comparisons of the segmentation results by using two voting strategies. The first row shows the ground truth. The second row is the segmentation results of hard voting strategy, and the third row is the segmentation results of soft voting strategy. (a) the segmentation results (the first row is the input image) (b) WM (c) GM (d) CSF.

VII. MERGING PROCESS

After fine-tuning, we get the segmented image amplified by n times. To recover the image to the original size, we down sample the image by using a merging strategy. We merge $n \times n$ pixels to one pixel from up to down and left to right without overlap. In the merging process, there are two situations:

(1) most pixels belong to cluster k_i;

(2) the number of pixels distributed to each cluster is same.

In situation (1), we merge the $n \times n$ pixels to cluster k_i according to the majority rule. In situation (2), we sum the membership of each pixel to each cluster, and distribute the pixels to the cluster whose total membership is maximum.

VIII. EXPERIMENTAL RESULTS

This section describes the segmentation results of our approach and other five algorithms, including FCM_S, FGFCM, EnFCM, FLICM and KWFLICM, on the simulative and real brain MR images. The real MR brain images are obtained from Qilu Hospital of Shandong University. The obvious differences in the segmentation results are marked by rectangles. The amplified rate n is set as 2 by experiences.

The size of neighboring local window in the global segmentation method is set as 3×3, same as those in FCM_S, FLICM and KWFLICM algorithms. The size of detection window in fine-tuning process is set as 6×6, and the reason will be stated in the next part.

FIGUREs 11, 12, and 13 present the brain MR images segmentation results of SFCMFT, FCM_S, FLICM, and KWFLICM, respectively. The three images are all from BrianWeb, and corrupted by 3%, 7%, 9% noises, respectively. The ground truth of each tissue is provided by Brainweb online. These ground truths of tissues are probabilistic maps. Here, we obtained the ground truth by retaining the pixels in each tissue whose gray values are larger than 0. Note that, for the overlapped pixels of different tissues, we distribute them to the tissues in which their gray values are larger (meaning higher probability). From FIGUREs 11, 12, and 13, we can get that the segmentation results by using FLICM and KWFLICM are not as accurate as the segmentation results by using SFCMFT. The inaccurate segmentation portions are marked by the rectangles. Specifically, the boundaries between gray matter and white matter at the occipital cortex are closer to the ground truth by using our SFCMFT, marked by the red rectangles in FIGURE 11, FIGURE 12 and FIGURE 13. The boundaries between the cerebrospinal fluid and gray matter at the frontal cortex are more similar to the ground truth by using SFCMFT, such as the portions marked by the green rectangles in FIGURE 11 and FIGURE 12.

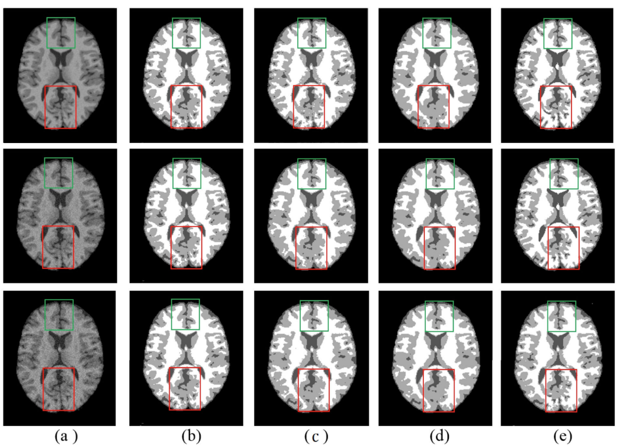

FIGURE 11. The results of brain MR image segmentation with 3%, 7%, 9% noise. (a) ground truth (b) FCM_S (c) FLICM (d) KWFLICM (e) SFCMFT.

In FIGURE 14, the first row shows the results of applying FCM_S, FLICM and SFCMFT on the brain MR images with 3% noise. The second to the fourth columns show the individual clusters obtained with the above algorithms respectively. The rows from top to bottom are membership functions of cerebrospinal fluid, gray matter and white matter, respectively. Compared with the ground truth (FIGURE 14(a)), it can be seen clearly that FLICM and KWFLICM cannot segment the tissue accurately, especially at the boundary between the white matter and gray matter,

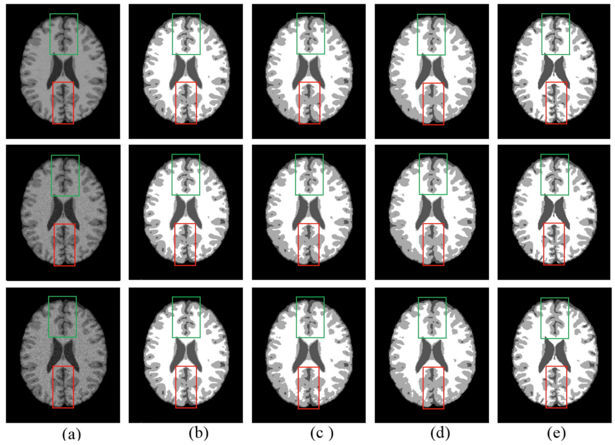

FIGURE 12. The results of brain MR image segmentation with 3%, 7%, 9% noise. (a) ground truth, (b) FCM_S, (c) FLICM, (d) KWFLICM, (e) SFCMFT.

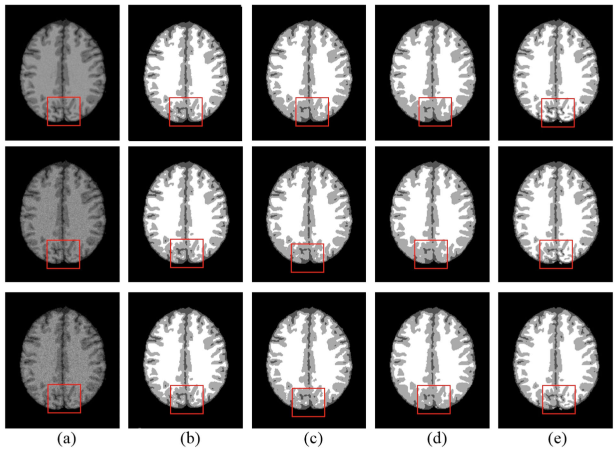

FIGURE 13. The result of brain MR image segmentation with 3%, 7%,9% noise. (a) ground truth, (b) FCM_S, (c) FLICM, (d) KWFLICM, (e) SFCMFT.

and the cerebrospinal fluid inside brain sulci. Due to the partial volume effect, the gray values of gray matter and white matter are very close. Moreover, the cerebrospinal fluid inside brain sulci is small and narrow, and it is easily confused with noise, as marked by the red rectangles in FIGURE 14. FLICM and KWFLICM do not pre-process the input brain MR image with noise, so the image is fuzzy and contains noise. In the segmentation process, due to the deficient use of local information, FLICM and KWFLICM cannot distinguish white matter from gray matter accurately, and cannot tell all the cerebrospinal fluid from the brain sulci. SFCMFT amplifies the image to reduce the effect of noises in the image and enhance the clarity of boundary between different tissues. Moreover, SFCMFT redefines the new fuzzy factor of the relationship between pixels and their neighbors by introducing the shape parameter and the anomaly detection parameter. SFCMFT can segment the gray matter and white matter, and distinguish the cerebrospinal fluid in brain sulci more accurately, which provides a reliable method for image-analysis and medical diagnosis.

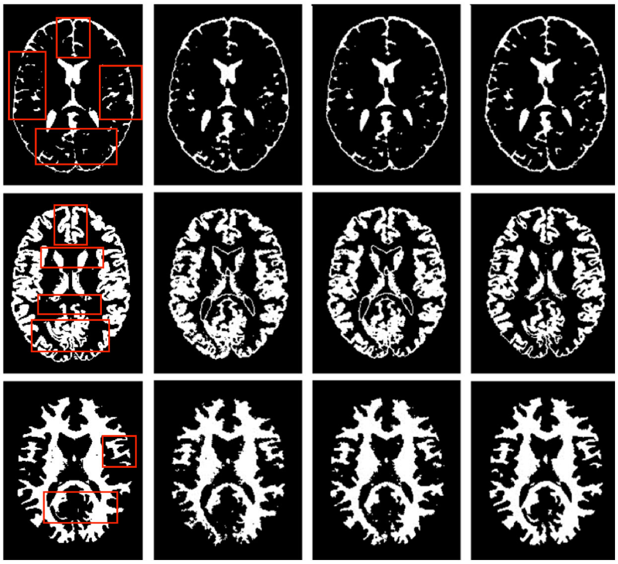

FIGURE 14. The result of brain MR segmentation result with 3% noise, from top to bottom is CSF, GM, WM. (a) ground truth (b) FCM_S (c) FLICM (d) SFCMFT.

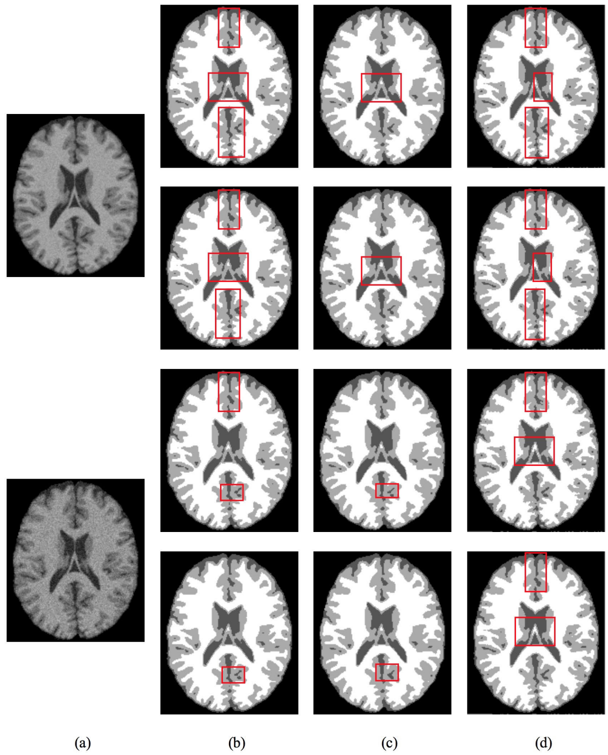

FIGURE 15. Segmentation results of medical image corrupted by 5% and 9%. (a) input image (b) FLICM (c) KWFLICM (d) SFCMFT. The first and third rows are results with fine-tuning, and the second and fourth rows are results without fine-tuning.

We apply the proposed fine-tuning post-processing on FLICM and KWFLICM algorithms, and compare with the segmentation result without fine-tuning, as shown in FIGUREs 15 and 16. Note that, in FIGUREs 15 and 16, the input images are the amplified images after the super-resolution process. The first and third rows are the results of FLICM, KWFLICM and SFCMFT with fine-tuning process, and the second and fourth rows are the results of FLICM, KWFLICM and SFCMFT without fine-tuning process. Fine-tuning utilizes the boundary details adequately, by re-segmenting the local windows around the boundary. Because the number of clusters in local windows is less, and the difference of gray values of pixels in the same cluster is smaller, it can avoid partial volume effect between different tissues to get an ideal result to some extent (the first and third rows in FIGURE 15 and FIGURE 16), as marked by red rectangles. These results show that the fine-tuning process can be applied to other segmentation algorithms, making it a general post-processing framework to improve the segmentation results.

FIGURE 17 shows the segmentation results of a real human brain MR image, effected by noise. To further segment the real brain MR image, we remove the skull in FIGURE 17 and apply SFCMFT on the image, as shown in FIGURE 18(b). FIGURE 18(c) is the ground truth segmented by brain experts manually. In this real brain MR image, the boundary between gray matter and cerebrospinal fluid is not clear, nor is the boundary between white matter and gray matter, causing inaccurate results. SFCMFT amplifies the input image to enhance the clarity of boundaries, and then judges the noise accurately by the introduced shape and anomaly detect parameters. The fine-tuning process re-assigns the pixel to its correct cluster around the boundary. Compared with the ground truth, SFCMFT can segment the tissues more accurately, especially the boundary between the gray matter and white matter and the boundary between the gray matter and cerebrospinal fluid, as marked by green and red rectangles, respectively.

Segmentation accuracy (SA) is adopted to evaluate the segmentation results quantificationally, which is defined as the sum of the pixels that are correctly classified divided by the number of all pixels. Formally,

$$SA = \sum\nolimits_{k=1}^{C} \frac{A_k \cap C_k}{\sum_{i=1}^{C} C_i}, \tag{12}$$

where A_k is the set of pixels belonging to the k class in the result, C_k is the set of pixels belonging to the k class in the reference image. Compared with the existing five algorithms, SFCMFT could get higher SAs, meaning that it performs better than other algorithms, as shown in TABLE 3.

We further adopt the popular measurements, dice similarity coefficient (DSC), sensitivity and specificity to quantitatively assess the performance of these segmentation algorithms. For each tissue, DSC, sensitivity and specificity are computed as follows:

$$DSC = \frac{2 \times TP}{TP + FP + FN}, \tag{13}$$

$$sensitivity = \frac{TP}{TP + FN}, \tag{14}$$

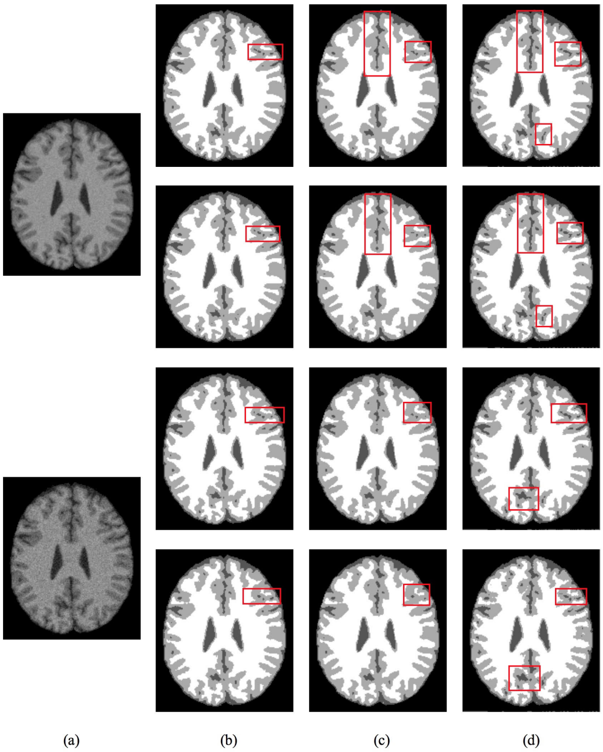

FIGURE 16. Segmentation results of medical image corrupted by 5% and 9% noise. (a) input image (b) FLICM (c) KWFLICM (d) SFCMFT. The first and third rows are results with fine-tuning, and the second and fourth rows are results without fine-tuning.

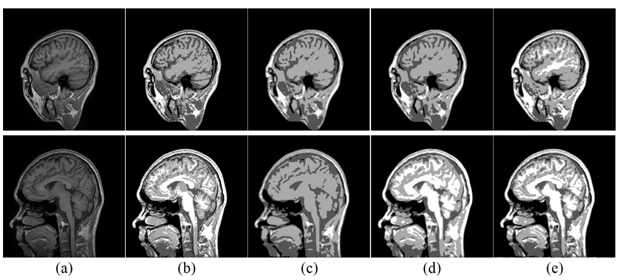

FIGURE 17. The real MR brain image. (a) input image (b) FCM (c) FLICM (d) KWFLICM (e) SFCMFT.

$$specificity = \frac{TN}{FP + FN}, \tag{15}$$

where FP, FN and TP are the numbers of false-positive, false-negative and true-positive voxels, respectively. The values of DSC, sensitivity and specificity range from 0 to 1, and high values mean more similarity to the ground truth. Compared with the existing five algorithms, SFCMFT could get higher DSCs, meaning that it performs better than other algorithms, as shown in TABLE 4. Note that, the DSCs in TABLE 4 are the average of DSCs of all tissues. The DSCs results of different tissues are shown in Tables 1-3 in the supplemental materials. Compared with the existing five algorithms, SFCMFT could get higher sensitivities and specificities, meaning that it get more pixels clustered rightly,

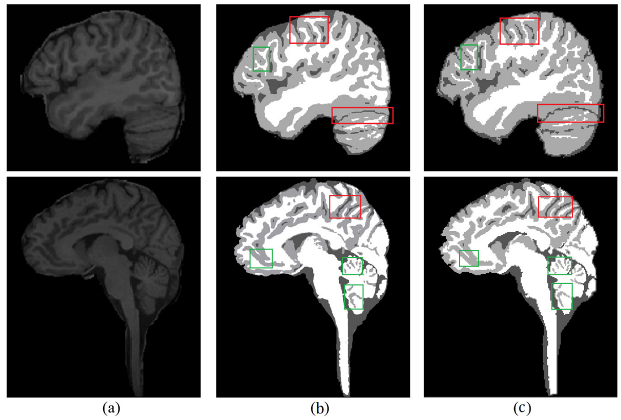

FIGURE 18. The results of real MR brain images without skull. (a) input image without skull (b) SFCMFT (c) ground truth.

TABLE 3. Comparison of SAs for brain images with noise.

Image	Noise	FCM_S	FGFCM	EnFCM	FLICM	KWFLICM	SFCMFT
FIG. 11	3% noise	0.951	0.925	0.937	0.979	0.946	0.995
	7% noise	0.925	0.910	0.916	0.947	0.929	0.973
	9% noise	0.921	0.889	0.897	0.931	0.914	0.960
FIG. 12	3% noise	0.932	0.895	0.912	0.976	0.947	0.983
	7% noise	0.927	0.883	0.901	0.964	0.938	0.967
	9% noise	0.908	0.867	0.888	0.942	0.916	0.952
FIG. 13	3% noise	0.943	0.911	0.923	0.967	0.947	0.993
	7% noise	0.926	0.905	0.912	0.939	0.928	0.969
	9% noise	0.914	0.882	0.896	0.921	0.899	0.952
FIG. 18	7% noise	0.746	0.591	0.690	0.722	0.825	0.884

while smaller pixels clustered wrongly, as shown in TABLE 5 and TABLE 6.

To further compare these algorithms, two cluster validity functions are selected for evaluation, which are the partition coefficient V_{pc} and the partition entropy V_{pe}, defined as follows:

$$V_{pc} = \sum_{k=1}^{C}\sum_{j=1}^{N} \mu_{kj}^2 / N, \tag{16}$$

$$V_{pe} = \sum_{k=1}^{C}\sum_{j=1}^{N} (\mu_{kj} \log \mu_{kj}) / N, \tag{17}$$

where N is the number of pixels in a given image, C is the number of classes. The final partition of the image with less fuzziness means a better performance. Hence, the best clustering is achieved when V_{pc} is maximal and V_{pe} is minimal. The partition coefficient V_{pc} and the partition entropy V_{pe} on the brain MR images are provided in TABLE 7 and TABLE 8, respectively. It is worth noting that the values of V_{pc} and V_{pe} are the average values of ten runs. As shown in

TABLE 4. Comparison of DSCs for brain images with noise.

Image	Noise	FCM_S	FGFCM	EnFCM	FLICM	KWFLICM	SFCMFT
	3% noise	0.886	0.850	0.867	0.899	0.896	0.926
FIG. 11	7% noise	0.867	0.836	0.851	0.884	0.890	0.901
	9% noise	0.847	0.798	0.794	0.865	0.871	0.890
	3% noise	0.889	0.863	0.873	0.902	0.910	0.929
FIG. 12	7% noise	0.876	0.851	0.858	0.887	0.897	0.923
	9% noise	0.863	0.820	0.835	0.883	0.888	0.900
	3% noise	0.891	0.867	0.874	0.911	0.916	0.941
FIG. 13	7% noise	0.879	0.854	0.865	0.900	0.907	0.932
	9% noise	0.872	0.834	0.851	0.887	0.894	0.925

TABLE 5. Comparison of sensitivities for brain images with noise.

Image	Noise	FCM_S	FGFCM	EnFCM	FLICM	KWFLICM	SFCMFT
	3% noise	0.883	0.838	0.854	0.892	0.931	0.953
FIG. 11	7% noise	0.858	0.825	0.840	0.868	0.916	0.928
	9% noise	0.835	0.787	0.801	0.856	0.879	0.909
	3% noise	0.877	0.861	0.862	0.905	0.917	0.936
FIG. 12	7% noise	0.859	0.849	0.843	0.876	0.896	0.919
	9% noise	0.847	0.818	0.832	0.863	0.869	0.892
	3% noise	0.900	0.857	0.877	0.916	0.924	0.949
FIG. 13	7% noise	0.880	0.850	0.854	0.894	0.917	0.922
	9% noise	0.868	0.824	0.843	0.883	0.882	0.903

TABLE 6. Comparison of specificities for brain images with noise.

Image	Noise	FCM_S	FGFCM	EnFCM	FLICM	KWFLICM	SFCMFT
	3% noise	0.878	0.849	0.859	0.889	0.880	0.903
FIG. 11	7% noise	0.866	0.828	0.840	0.866	0.865	0.876
	9% noise	0.853	0.779	0.789	0.831	0.842	0.866
	3% noise	0.894	0.846	0.868	0.894	0.900	0.915
FIG. 12	7% noise	0.868	0.838	0.841	0.851	0.872	0.892
	9% noise	0.841	0.800	0.799	0.832	0.843	0.865
	3% noise	0.897	0.853	0.879	0.895	0.899	0.917
FIG. 13	7% noise	0.886	0.833	0.858	0.881	0.874	0.891
	9% noise	0.857	0.810	0.844	0.854	0.862	0.886

TABLE 7 and TABLE 8, the V_{pc} and V_{pe} values of SFCMFT are comparable to or even better than those of the other algorithms on the brain MR image contaminated by noise with varying degrees.

The time complexity of SFCMFT is $O((\frac{n}{r+1})^2 CI)$, where I is the number of iterations and r is the size of the detection

TABLE 7. Comparison of V_{pc}.

Image	Noise	FCM_S	FGFCM	EnFCM	FLICM	KWFLICM	SFCMFT
	3% noise	0.882	0.823	0.893	0.912	0.879	0.945
FIG. 11	7% noise	0.862	0.887	0.827	0.893	0.863	0.930
	9% noise	0.897	0.794	0.892	0.839	0.873	0.916
	3% noise	0.869	0.820	0.913	0.917	0.870	0.934
FIG. 12	7% noise	0.897	0.883	0.902	0.882	0.872	0.921
	9% noise	0.918	0.815	0.889	0.889	0.837	0.890
	3% noise	0.907	0.804	0.914	0.925	0.919	0.965
FIG. 13	7% noise	0.891	0.853	0.906	0.911	0.891	0.958
	9% noise	0.872	0.896	0.899	0.894	0.883	0.922
FIG. 18	7% noise	0.813	0.844	0.785	0.847	0.899	0.907

TABLE 8. Comparison of V_{pe}.

Image	Noise	FCM_S	FGFCM	EnFCM	FLICM	KWFLICM	SFCMFT
	3% noise	0.347	0.295	0.331	0.274	0.362	0.165
FIG. 11	7% noise	0.381	0.318	0.352	0.292	0.326	0.202
	9% noise	0.412	0.404	0.404	0.320	0.388	0.269
	3% noise	0.932	0.214	0.214	0.266	0.338	0.107
FIG. 12	7% noise	0.927	0.279	0.279	0.306	0.367	0.230
	9% noise	0.908	0.306	0.306	0.331	0.403	0.293
	3% noise	0.943	0.342	0.358	0.312	0.329	0.183
FIG. 13	7% noise	0.926	0.481	0.390	0.375	0.393	0.194
	9% noise	0.914	0.423	0.442	0.431	0.459	0.258
FIG. 18	7% noise	0.746	0.569	0.497	0.401	0.394	0.329

window. Therefore, it is not reasonable to assign too small value to the r considering the complexity of computing. However, a small r is needed to enhance the accuracy of fine-tuning. The line chart in FIGURE 19 shows the change of the SA values with different window sizes r.

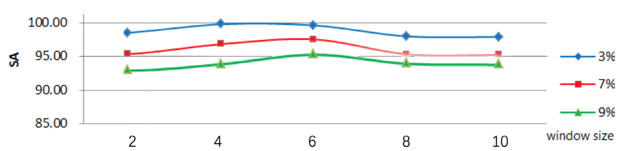

FIGURE 19. Line graph of SA with the change of size of the window.

When r is set to 2, the accuracy is still effected by noise. The higher the noise level is, the lower the accuracy becomes, as shown by the red and green lines in FIGURE 19. When r is set to 8 or larger, the enhancement of accuracy is not obvious. In the image effected by little noise, there is no obvious difference between setting r as 4 and 6, as shown by the blue line in FIGURE 19. However, when the noise is heavy, setting r as 6 could achieve more accurate results, as shown by the green and red lines in FIGURE 19. Therefore, in our fine-tuning process, r is set as 6.

IX. CONCLUSION

In this paper, we design a general framework SFCMFT for brain MR image segmentation. Firstly, we use a cubic surface fitting algorithm to pre-process the original brain MR image, which can smooth out noise meanwhile improving image clarity. Secondly, we design a new fuzzy factor by introducing a shape parameter and an anomaly detection parameter to control the trade-off between noise removal and detail preservation more accurately. Lastly, we propose a fine-tuning process, to re-segment the detection windows near boundary and refine the incorrect pixels. Experimental results by applying our techniques to various brain MR images show that SFCMFT can improve the accuracy and robustness of the brain MR image segmentation. However, SFCMFT has a higher running time and the result of fine-tuning process depends on the global segmentation to some extent, as shown in Table 4 in the supplemental materials, which we plan to address in the future. Moreover, we do not consider the skull or other structures in MR images (whose gray values are close to the gray values of tissues, as shown in FIGURE 17). In the future, we will improve our method to perform on the whole brain with skull structures. Furthermore, our research focuses on the brain MR images affected by natural noise, which is similarly governed by a Rician distribution. In the future, we will improve our method for other noises.

REFERENCES

[1] J. Xia, F. Wang, Z. Wu, L. Wang, C. Zhang, D. Shen, and G. Li, "Mapping hemispheric asymmetries of the macaque cerebral cortex during early brain development," *Human Brain Mapping*, vol. 41, no. 1, pp. 95–106, Jan. 2020.

[2] A. Halder and N. A. Talukdar, "Robust brain magnetic resonance image segmentation using modified rough-fuzzy C-means with spatial constraints," *Appl. Soft Comput.*, vol. 85, Dec. 2019, Art. no. 105758.

[3] N. Mahata, S. Kahali, S. K. Adhikari, and J. K. Sing, "Local contextual information and Gaussian function induced fuzzy clustering algorithm for brain MR image segmentation and intensity inhomogeneity estimation," *Appl. Soft Comput.*, vol. 68, pp. 586–596, Jul. 2018.

[4] L. Wang *et al.*, "Benchmark on automatic six-month-old infant brain segmentation algorithms: The iSeg-2017 challenge," *IEEE Trans. Med. Imag.*, vol. 38, no. 9, pp. 2219–2230, Sep. 2019.

[5] Z. Wang, L. Guo, S. Wang, L. Chen, and H. Wang, "Review of random walk in image processing," *Arch. Comput. Methods Eng.*, vol. 26, no. 1, pp. 17–34, Jan. 2019.

[6] C. Singh and A. Bala, "A transform-based fast fuzzy C-means approach for high brain MRI segmentation accuracy," *Appl. Soft Comput.*, vol. 76, pp. 156–173, Mar. 2019.

[7] C. Wu and X. Yang, "Robust credibilistic fuzzy local information clustering with spatial information constraints," *Digit. Signal Process.*, vol. 97, Feb. 2020, Art. no. 102615.

[8] J. P. Sarkar, I. Saha, and U. Maulik, "Rough possibilistic type-2 fuzzy C-means clustering for MR brain image segmentation," *Appl. Soft Comput.*, vol. 46, pp. 527–536, Sep. 2016.

[9] J. Miao, X. Zhou, and T.-Z. Huang, "Local segmentation of images using an improved fuzzy C-means clustering algorithm based on self-adaptive dictionary learning," *Appl. Soft Comput.*, vol. 91, Jun. 2020, Art. no. 106200.

[10] Y. Zhang, X. Bai, R. Fan, and Z. Wang, "Deviation-sparse fuzzy C-means with neighbor information constraint," *IEEE Trans. Fuzzy Syst.*, vol. 27, no. 1, pp. 185–199, Jan. 2019.

[11] D. Kumar, H. Verma, A. Mehra, and R. K. Agrawal, "A modified intuitionistic fuzzy C-means clustering approach to segment human brain MRI image," *Multimedia Tools Appl.*, vol. 78, no. 10, pp. 12663–12687, May 2019.

[12] M. N. Ahmed, S. M. Yamany, N. Mohamed, A. A. Farag, and T. Moriarty, "A modified fuzzy C-means algorithm for bias field estimation and segmentation of MRI data," *IEEE Trans. Med. Imag.*, vol. 21, no. 3, pp. 193–199, Mar. 2002.

[13] K.-S. Chuang, H.-L. Tzeng, S. Chen, J. Wu, and T.-J. Chen, "Fuzzy C-means clustering with spatial information for image segmentation," *Comput. Med. Imag. Graph.*, vol. 30, no. 1, pp. 9–15, Jan. 2006.

[14] X. Zhang, C. Zhang, W. Tang, and Z. Wei, "Medical image segmentation using improved FCM," *Sci. China Inf. Sci.*, vol. 55, no. 5, pp. 1052–1061, May 2012.

[15] L. Szilagyi, Z. Benyo, S. M. Szilagyi, and H. S. Adam, "MR brain image segmentation using an enhanced fuzzy C-means algorithm," in *Proc. 25th Annu. Int. Conf. IEEE Eng. Med. Biol. Soc.*, vol. 1, Sep. 2003, pp. 724–726.

[16] W. Cai, S. Chen, and D. Zhang, "Fast and robust fuzzy C-means clustering algorithms incorporating local information for image segmentation," *Pattern Recognit.*, vol. 40, no. 3, pp. 825–838, Mar. 2007.

[17] S. Krinidis and V. Chatzis, "A robust fuzzy local information C-means clustering algorithm," *IEEE Trans. Image Process.*, vol. 19, no. 5, pp. 1328–1337, May 2010.

[18] M. Gong, Y. Liang, J. Shi, W. Ma, and J. Ma, "Fuzzy C-means clustering with local information and kernel metric for image segmentation," *IEEE Trans. Image Process.*, vol. 22, no. 2, pp. 573–584, Feb. 2013.

[19] Y. Kong, J. Wu, G. Yang, Y. Zuo, Y. Chen, H. Shu, and J. L. Coatrieux, "Iterative spatial fuzzy clustering for 3D brain magnetic resonance image supervoxel segmentation," *J. Neurosci. Methods*, vol. 311, pp. 17–27, Jan. 2019.

[20] S. N. Kumar, A. L. Fred, and P. S. Varghese, "Suspicious lesion segmentation on brain, mammograms and breast MR images using new optimized spatial feature based super-pixel fuzzy C-Means clustering," *J. Digit. Imag.*, vol. 32, no. 2, pp. 322–335, Apr. 2019.

[21] Z. Caiming, Z. Xin, L. Xuemei, and C. Fuhua, "Cubic surface fitting to image with edges as constraints," in *Proc. IEEE Int. Conf. Image Process.*, Sep. 2013, pp. 1046–1050.

[22] J. Yang, Z. Lin, and S. Cohen, "Fast image super-resolution based on in-place example regression," in *Proc. IEEE Conf. Comput. Vis. Pattern Recognit.*, Jun. 2013, pp. 1059–1066.

[23] R. Timofte, V. De, and L. V. Gool, "Anchored neighborhood regression for fast example-based super-resolution," in *Proc. IEEE Int. Conf. Comput. Vis.*, Dec. 2013, pp. 1920–1927.

[24] R. Timofte, V. De Smet, and L. Van Gool, "A+: Adjusted anchored neighborhood regression for fast super-resolution," in *Proc. Asian Conf. Comput. Vis.* Springer, 2014, pp. 111–126.

[25] M. Ren, Z. Wang, and J. Jiang, "A self-adaptive FCM for the optimal fuzzy weighting exponent," *Int. J. Comput. Intell. Appl.*, vol. 18, no. 2, Jun. 2019, Art. no. 1950008.

JING XIA (Associate Member, IEEE) received the Ph.D. degree from the School of Computer Science and Technology, Shandong University, in 2019. Her research interests include brain MR image segmentation, early brain cortex development, parcellation of brain cortical surface, and medical image segmentation.

XUEMEI LI is currently an Associate Professor with the School of Computer Science and Technology, Shandong University. Her research interests include image denoise, machine learning, and so on.

GUONING CHEN received the Ph.D. degree in computer science from Oregon State University, in 2009. He worked as an Instructor with the Computer Science Department, Guangxi University, from 2002 to 2004. He was a Postdoctoral Researcher with the Scientific Computing and Imaging (SCI) Institute, University of Utah, from 2009 to 2012. He is currently an Associate Professor with the Department of Computer Science, University of Houston.

CAIMING ZHANG received the B.S. and M.E. degrees in computer science from Shandong University, in 1982 and 1984, respectively, and the Dr. Eng. degree in computer science from the Tokyo Institute of Technology, Japan, in 1994. From 1997 to 2000, he has held visiting position with the University of Kentucky, USA. He is currently a Professor and the Ph.D. Supervisor with the School of Computer Science and Technology, Shandong University. He is also the Dean and a Professor with the School of Computer Science and Technology, Shandong University of Finance and Economics. His research interests include CAGD, CG, information visualization, and medical image processing.